Identification of damage-induced frequency decay on a large-scale model bridge

(Article begins on next page)

15 August 2024

Investigation of damage-induced frequency decay on a large scale model bridge

Mirco Tarozzi [a]*, Giacomo Pignagnoli [a], Andrea Benedetti [a]

a) Department of Civil, Chemical, Environmental and Materials Engineering, University of Bologna, Viale Risorgimento 2, 40136 Bologna, Italy.

* Corresponding author.

Phone: +39 051 2093235

Email: mirco.tarozzi4@unibo.it

Abstract – Planning the maintenance activity of a civil structure with a life cycle cost-effectiveness requires the evaluation of its functionality in service to identify possible damage states which need a retrofit, avoiding thus danger for the users. In this paper, this topic is explored by using an experimental 1:4 scale model bridge, in which some damage states on the main steel beams are introduced arbitrarily with the aim of detecting the effect of local cracks on the performance of the structure. By performing dynamic tests on the model bridge, it was possible to link the variability of the natural frequencies with the gradual stiffness reduction caused by the cracks. By processing the acceleration signals due to a random excitation of the 6.0×3.0 m^2 deck, the main natural frequencies of the bridge have been extracted in several progressive damage states. The observed behaviour was explained by making use of a detailed Finite Elements numerical model. The frequency decay predicted by these methods is in close agreement with the experimental observations and permits to build a useful link between frequency data and damage detection.

Keywords: Damage detection, Dynamic test, Frequency shift, Operational Modal Analysis, Composite Bridge, Cracked Beam.

1 Introduction

The prediction of the evolving strength and the structural integrity of strategic structures, such as hospitals, rescue buildings or bridges, has attracted the interest of many researchers. Their performance can be shattered by environmental and accidental actions and therefore in the order of avoiding the

1

32 suspension of the service state, early detection of the damaged condition is

33 mandatory.

34 Since the last few years of the 20th Century, several non-destructive tests became

35 available to assess the mechanical properties of the materials [1, 2]. Concerning

36 masonry and timber, the authors have recently examined a procedure to

37 characterize them or their health condition [3, 4]. The use of non-destructive

38 methods to estimate the actual health condition of bridges and other civil

39 structures is still in progress and subject of many studies [5, 6]

40 Unfortunately, often the elements to be tested are not easily attainable, and the

41 material properties can vary inside the structure and among subsequent

42 investigations, causing thus uncertainty in damage estimation. In any case, those

43 methods cannot be used as a continuous process able to show the evolution of

44 the health state of the structure.

45 In the last years, the collection and the processing of the ambient vibrations

46 became one of the main experimental methods for a global condition assessment

47 of structures through the identification of their dynamic behaviour.

48 The Operation Modal Analysis (OMA) algorithms have been developed both in

49 the frequency domain and in the time domain to identify main natural

50 frequencies, damping ratios, and mode shapes [7, 8, 9]. The outcomes of

51 different identification techniques, for instance, the Frequency Domain

52 Decomposition (FDD) method [10, 11, 12] and the Stochastic Subspace

53 Identification (SSI) method [13, 14, 15] yield consistent cross-correlated

54 information for the optimization of the finite element (FE) models.

55 Usually, global modal parameters are functions of the physical properties of the

56 structure. Thus, changes in the physical properties of the structure induce

57 variation in the modal parameters. The topic is still the subject of continuous

research [16, 17, 18, 19] aiming at the characterization of the damages in terms of position and intensity. Many tests were carried out almost twenty years ago on full-scale structures and created a solid baseline for the research in the fields of vibration-based Structural Health Monitoring (SHM) and Damage Detection (DD) [20, 21, 22, 23, 24]. The data collected performing those tests are often used as benchmark developing new algorithms or comparing the detection capability and the robustness of different damage indicators [25]. Other methods for detecting damage are currently in progress, taking advantage either of modal strains measured by optical fibres [26] or of recent advances in the information technology, mainly involving artificial neural networks and machine learning approaches [27, 28].

Most of the cited activities used decommissioned bridges in which localized damage scenarios were produced by cutting concrete or steel parts. Lauzon et Al. [29] presented an investigation similar to the one shown here but acting progressively only on one beam. Zhou & Biegalski [30] studied a real damaged bridge with a damage scenario very similar to the one used in the model bridge, but no dynamic investigation was performed. Hagani et Al. [31] listed several damage patches detected in real bridges but any link with the change of dynamic properties was set out. Chajes et Al [32] detailed the damage detected in the I-95 Delaware bridge and the restoration works, but information concerning the bridge stiffness variation is missing.

However, the cited experiments allowed only episodic data collection not linked with the loading level experienced by the bridge. A laboratory scaled model can be loaded and dynamically investigated repeatedly at different load levels, ages, corrosion extent, etc., building so representative correlations of the parameters describing the state, and allowing for future further checks of the extracted data.

84   Therefore the present study aims to evaluate how local damages, increasing in

85   their severity, influence the natural frequency of a bridge. This is done by

86   assessing the loss of stiffness from frequency decays but neglecting the influence

87   of the damage position.

88   In particular, the studied experimental model permitted not only to gather a wide

89   set of data in several bridge damage configurations but through the comparison

90   with a 3D FE model did establish a link between the dynamic properties and the

91   damage features which will be useful in planning the condition assessment

92   through dynamic monitoring of real deteriorated full-scale bridges.

93   Usually, The cost of the monitoring networks installed on most of the highways

94   and civil structures is strongly influenced by the physical characteristic, the level

95   of quality in terms of sensor' technology and number involved in each network.

96   Concerning the total cost of this kind of networks, the use of a huge number of

97   high-sensitive sensors, their installation and the management of the recorded

98   data may prove to be too expensive for the Public Administration that asks for

99   the service, especially for networks designed for permanent monitoring.

100   The solution to this problem is to use a proper number of low-cost sensors

101   evenly distributed on the structure or, in other cases, the use of high-sensitive

102   sensors placed at key locations. Limiting the number of sensors is the solution

103   considered in this paper, owing to reduce the network costs and the amount of

104   recorded data as much as possible.

105

106

107

108

2 EXPERIMENTAL TEST

2.1 Description of the tested bridge model

The composite steel-concrete bridge deck under study is the 1:4 scaled model of an existing bridge crossing the A14 highway in Italy, near the city of Bologna (Figure 1). The scaling phase involved only the geometrical dimension, whereas the properties of the materials were selected according to the common design practice.

Figure 1. The bridge crossing the A14 highway (on the left) and the scaled model under investigation (on the right).

The model was designed as a tool for checking the ability of dynamic tests in detecting localized damage states. The evaluation was carried out by means of a comparative 3D FE model featuring all the details of the experimental bridge. The performance of the model was calibrated by using a static 4 Point Bending Test (4PBT) as a reference. Then, the prepared FE model was used as a simulation tool in predicting the effect of different damage scenarios.

The construction details and the geometrical data of the model bridge are described in the following. The strength classes and mechanical properties of the materials employed in the construction are summarized in Table 1.

128 The concrete was obtained with 350 kg/m^3 of Portland cement CEM II/A-LL

129 42.5R, a water-cement ratio varying from 0.53 to 0.59, sand in the range 0.1-1

130 mm and gravel in the range 5-15 mm complying to a granulometric curve for

131 thin sections. In agreement with the European Standard EN 206 [33], the poured

132 concrete achieved the strength class C28/35 with a density ρ equal to 2300

133 kg/m^3. The cubic compressive strength R_{ck} determined by laboratory tests held

134 38 MPa. The density was derived by weighing cubic samples. Then, ultrasonic

135 tests were performed on the same specimens to obtain an experimental value of

136 the dynamic elastic modulus. The concrete Young's modulus was finally

137 computed from the dynamic modulus with a mean value roughly equal to 25000

138 MPa.

139

140 Table 1. Mechanical properties of the construction materials employed in
141 the erection of the bridge and applied to the FE model of the bridge.

Material	Strength Class	Thickness [mm]	Elastic Modulus [MPa]	Density [kg/m^3]
Structural Steel[1]	S 275	Various	210000	7860
Concrete[2]	C 28/35	130	25000	2400*
Steel Rebar	B 450 C	Ø 8	210000	7860
Corrugated Steel[1]	S 275	0.8	210000	7860
Neoprene Sheet	Shore A	15	2.5	1270
Asphalt	-	25	-	800

[1] European Standard EN 10025 and EN 10219 [34, 35]

[2] European Standard EN 206 and UNI-EN 11104 [33]

* The density includes roughly 100 kg/m^3 of steel reinforcement.

142

143 The bridge is composed of two concrete abutments and a composite deck. Two

144 concrete walls raise from a piled raft foundation made of concrete. The

145 foundations are constrained by six Tubfix piles with a diameter of 127 mm and a

146   length of 6000 mm. The two piers are 3000 mm wide, 1500 mm high and 400

147   mm thick; such dimensions allow neglecting the piers' contribution to the bridge

148   deck dynamic behaviour.

149   The deck concrete slab is 6000 mm long and 3000 mm wide. A 55 mm tall stay-

150   in-place zinc-coated structural corrugated steel sheet formwork was adopted to

151   contain the concrete pouring, leading to an average total slab thickness of 130

152   mm. The slab reinforcement was set out with a bidirectional ø6/100 mm steel

153   mesh and ø8 transversal steel bars placed every 200 mm inside the ribs of the

154   corrugated steel sheet. After the bridge completion, the concrete slab was

155   finished with 25 mm of asphalt (Figure 2, Figure 3).

156   The steel braced framework illustrated in Figure 4 is fully made of steel S275

157   and includes three IPE 300 girders, two secondary cross girders made by

158   coupling two UNP 140 and six L 35x4 equal leg angles as cross bracings. Two

159   IPE 300 girders were used as head beams resting over the deck bearings laying

160   on the piers according to the longitudinal section of the bridge showed in Figure

161   2. The steel framework and the concrete deck are connected by rows of Nelson's

162   shear studs welded every 100 mm over the beam upper flanges.

163   The bridge deck is sustained by six 15 mm neoprene bearings, posed under the

164   head beams centred to the axis line of the main beams.
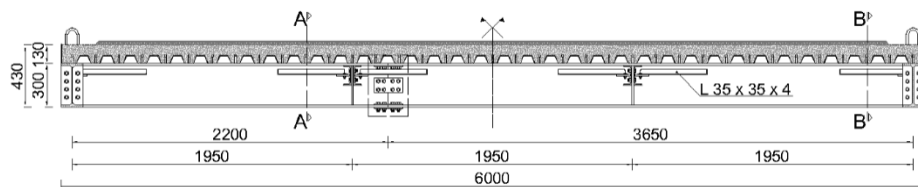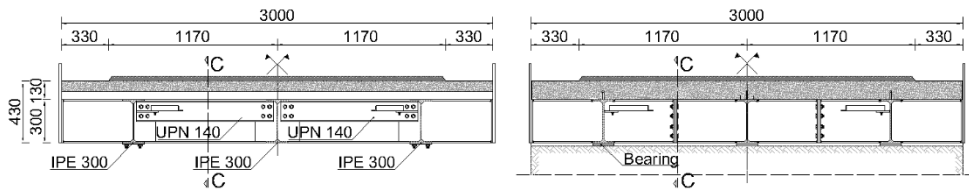
165

166   Figure 2. Longitudinal vertical section C-C of the steel deck.
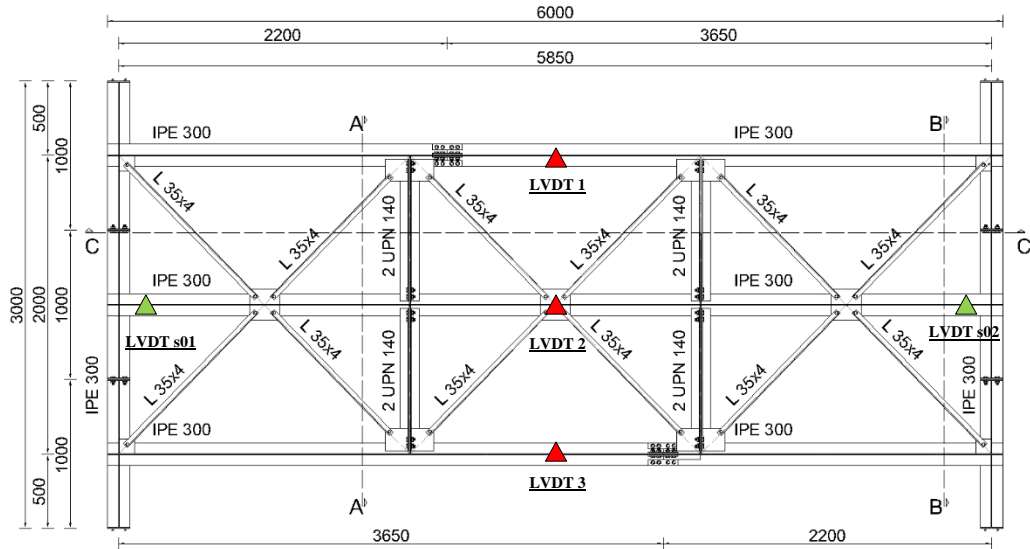
167

168

169   Figure 3. Transverse vertical sections A-A and B-B of the steel deck.


170

171   Figure 4. Plan view of the steel grillage and the position of the LVDTs adopted for the static load

172   test (measurement range: red marks 0-50 mm, green marks 0-20 mm).

173   During the construction phase and the deck casting operation, the structure was

174   not propped. For this reason, the concrete slab shows a non-uniform thickness

175   over its surface due to the uneven deflection of the steel elements. As a concern,

176   the tapered thickness of the slab is causing a frequency shift and switch due to

177   the changed mass distribution, requiring thus very precise modelling if the fit

178   with the experiments is the goal.

179   As usual, the connection among the main girders and the two head beams was

180   executed with welded joints, while bolted connections linked the secondary

181   cross girders and the bracings together to the main beams. Besides, two more

182   bolted twin plate splices illustrated in Figure 4 and Figure 5 were properly

183   designed for the outer main girders for both the web and the lower flange. These

184   joints were introduced to obtain full continuity, flange break or beam break in

185   one or two beams of the bridge steel framework, encompassing finally five

186   different simulated damage states.

187
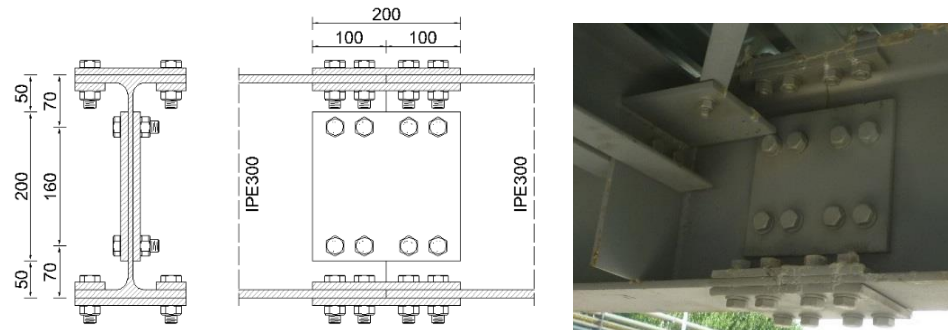
189 Figure 5: Bolted twin plate splices at one-third of the main beam length.

190

191   Naming "D0" the undamaged fully fastened condition, all the following steps

192   consisted in removing a bolted joint of a beam: "D1" means removing the lower

193   flange link on one beam; "D2" refers to the condition in which both flange and

194   web links were removed from the same beam; finally, "D3" and "D4" consisted

195   in replicating the same operations of D1 and D2 on the other outer beam.

196

197   2.2   Experimental Setup for Static Test

198   The setup designed for the static test is shown in Figure 6 and Figure 7. The

199   loading beam is composed of two IPE 500 profiles linked by pairs of UPN 300

200   elements. Two jacks with a capacity of 667 kN act on the beam' ends using

201   Dywidag rods with a diameter of 36 mm running inside the slots of the UPN 300

202   pairs. The reaction points are set with two pairs of Tubfix piles with diameter Ø

203   127 mm and length L = 10000 mm designed to balance the maximum forces

204 applied by the two hydraulic jacks. The beam was properly designed by a

205 stiffness criterion, to minimize its deformation during loading.

206

207

208 Figure 6: Static load test setup: on the left is shown the static loading system; on the right is

209 visible the data acquisition system.

210 Since in the bridge deck there are three main beams and the loading is performed

211 by a pair of beams, there are on the deck six loading points (Figure 7).

212 The maximum load applied on the bridge didn't lead to the yielding of the steel

213 members. Thus, the behaviour of the small bridge during the loading phase can

214 be considered fully linear elastic. The linear elastic behaviour allowed to

215 estimate the force exerted by each loading point simply by solving the static

216 scheme of the problem. By considering the huge stiffness of the loading beam,

217 the force acting at each concrete block can be computed following the

218 equilibrium equations governing the whole loading system. Because of the

219 skewness of the loading setup, the forces exerted on the loading points were

220 different. In particular, for each load step, the forces computed at each pair of

221 concrete cubes resulted in the 21%, 33% and 46% of the total applied load P for

222 the beams instrumented with the Linear Variable Differential Transducers

223 (LVDT's) 1, 2 and 3 respectively.
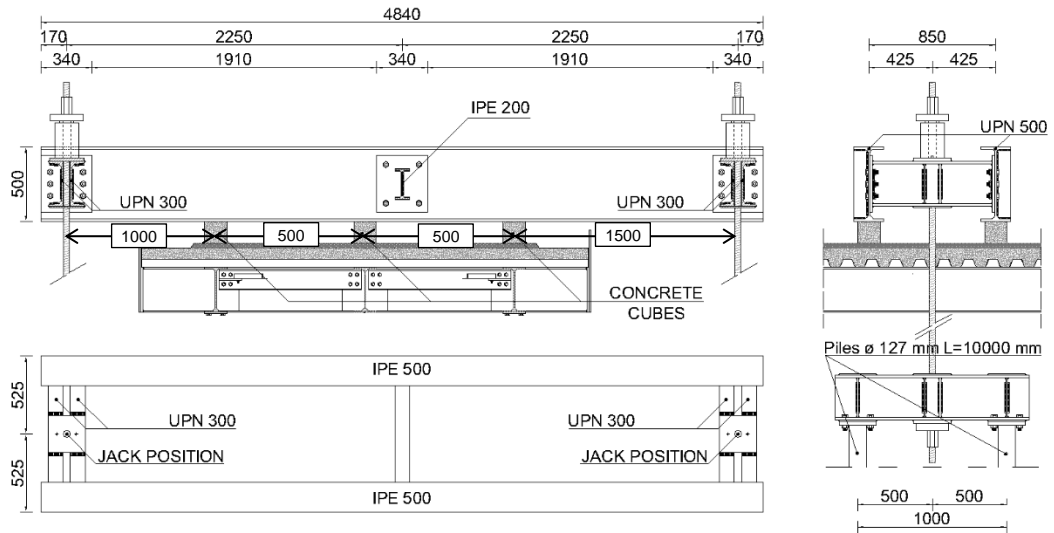
Figure 7: Drawings of the setup of the loading system.

During the experimental campaign, a total of 5 LDTV's recorded the displacements at the five marked positions of Figure 4, while a digital manometer measured the oil pressure provided to the two hollow jacks illustrated in Figure 6 and Figure 7. While three LVDTs (1 to 3) with a measuring range of 50 mm were placed below the mid-span of the main beams, the last two were placed near the supports measuring the deflection of the elastic bearings. The two LVDTs "s01" and "s02" were selected with a range of 20 mm to improve the accuracy of the measure.
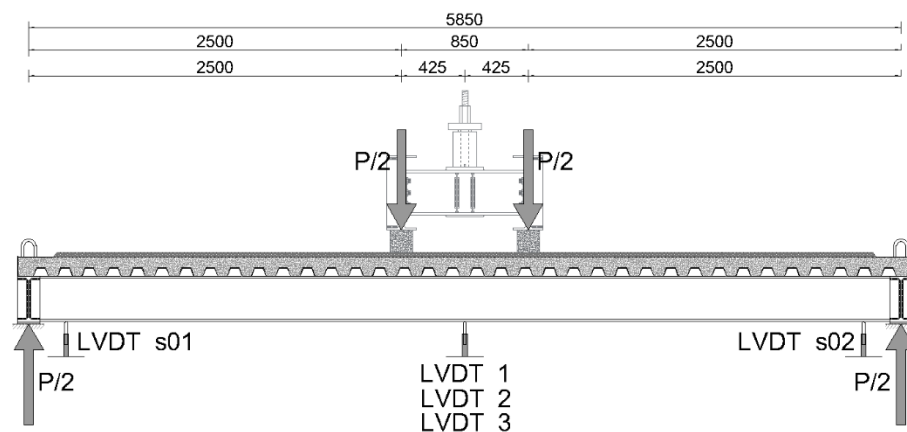

Figure 8: Setup for the static test.

238

2.3 Experimental Setup for Dynamic Test

240 The main frequencies, damping ratios, and modal shapes were extracted by

241 testing the bridge dynamically taking advantage of the ambient vibrations (AV),

242 a random people walk (RW) and hammer hit (HH) excitations.

243 Accelerations were measured at a sampling rate of 2000 Hz with a set of eight

244 tri-axial Sensr CX-1 mems accelerometers arranged according to the setup of

245 Figure 9. The CX-1 is an accelerometer developed by SENSR using the MEMS

246 technology, and it can measure the acceleration with the resolution of 10^{-6} g

247 within the range $\pm$ 1.5g. This sensor was widely used by the authors [36, 37, 38]

248 for other experimental campaigns, and performed very well in all environmental

249 conditions.
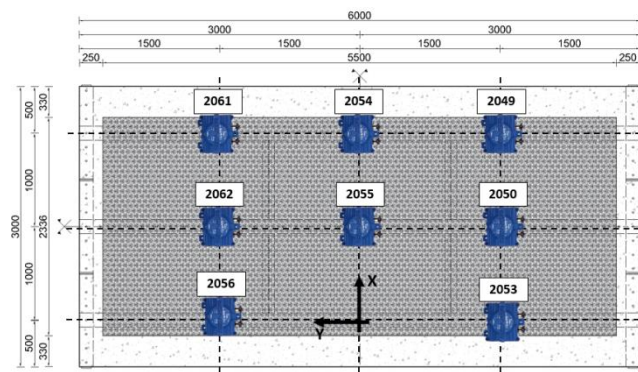
250

251

Figure 9: Setup used for the dynamic test.

252 Although composite steel-concrete decks are orthotropic plates, it is common

253 practice for the dynamic investigation to align many sensors on the axis line of

254 the bridge, while few of them are placed on transversal rows, owing to the

255 detection of torsional modes. In this experimental model, a grid-shape

256 arrangement of the sensors was chosen (Figure 9). Even if by using a greater

257 number of sensors or taking advantage of a multi-setup technique [39, 40] the

258   spatial resolution of the mode shapes and their representation could be

259   improved, the selected minimal setup was able to detect and clearly distinguish

260   the first six mode shapes of interest.

261   According to the capacity of the recording system, eight CX-1 [41] were used

262   during the initial dynamic identification stage, whereas in the following phases

263   only two accelerometers were employed, considering this setup as typical of

264   continuous damage monitoring in simple bridges. In particular, only the CX-1

265   named 2056 and 2049 were adopted for the dynamic investigation at each stage

266   of damage realization. These sensors were fixed on the lower flange of the two

267   external beams at a quarter of their length (Figure 10).

268
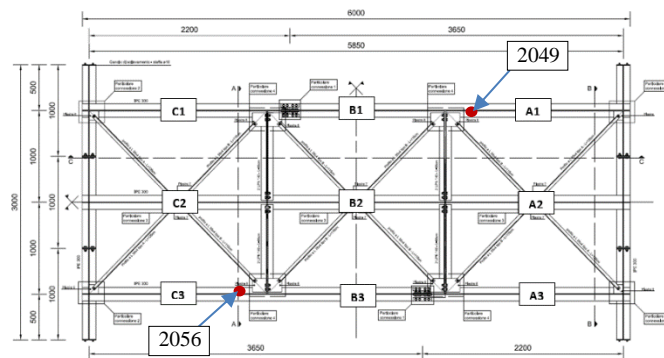
270   Figure 10. Accelerometers configuration in case of damage stages

271

272   All the measurements were performed repeatedly to improve the reliability of

273   the extracted modal parameters. All the tests were completed in a few days with

274   the same daily schedule, aiming to reduce the effect of the environmental

275   conditions. The temperature, roughly equal to 30°C, was the same for all the

276   tests.

277

278

2.4 Experimental Test Procedure

Once the early version of the FE model was created by following the technical drawings and assigning to the elements the nominal values of specific weight and Young's modulus given by the Italian Standards [42], the experimental tests followed three main steps. Firstly, the dynamic tests were performed to characterize the bridge at its undamaged condition by extracting modal frequencies, modal shapes, and damping ratios; secondly, the static tests allowed estimating the actual static stiffness of both the deck and the rubber bearings. Finally, repeated dynamic tests were carried out after each step of damage from D1 to D4.

According to the setup showed in the previous section, AV and RW excitations were recorded for 30 minutes and 8 minutes respectively, to ensure an acquisition window of at least 2000 times the fundamental period of the bridge. Then, one rubber hammer was used to perform HH excitation in different positions, triggering in this way a large number of the main dynamic modes. Finally, the time series were processed either considering the total length of the signal or processing the acceleration produced by each hammer hit singularly. Since this paper is devoted to investigating the influence of damage on the bending stiffness of the bridge and no significant difference was observed among the frequencies extracted from all the used excitation methods, only the lower main frequencies were extracted and their experimental values were defined by the average of all the completed tests.

The static loading consisted of three sets of ten load cycles starting from 0 kN up to 45 kN, 90 kN, and 140 kN respectively. The bridge was not damaged during the load cycles and its behaviour remained elastic throughout the tests.

3 The Finite Element Model

306   This section illustrates the numerical model of the bridge and the criteria

307   followed to set out proper values of the boundary condition at the supports. The

308   model was solved with the Italian version of the commercial FE software

309   STRAND.

310   All the mechanical properties of the employed materials are collected in Table 1.

311   Concerning the concrete, the properties were firstly estimated by performing

312   non-destructive tests (NDT) and then inserted into the numerical model. By

313   combining the reference properties given by the Italian Standards [42] and the

314   outcomes provided by NDT data, the starting FE model of the bridge was

315   created.

316   The sketch of the numerical model is provided in Figure 11, in which each

317   different colour means different mechanical properties assigned to the element.
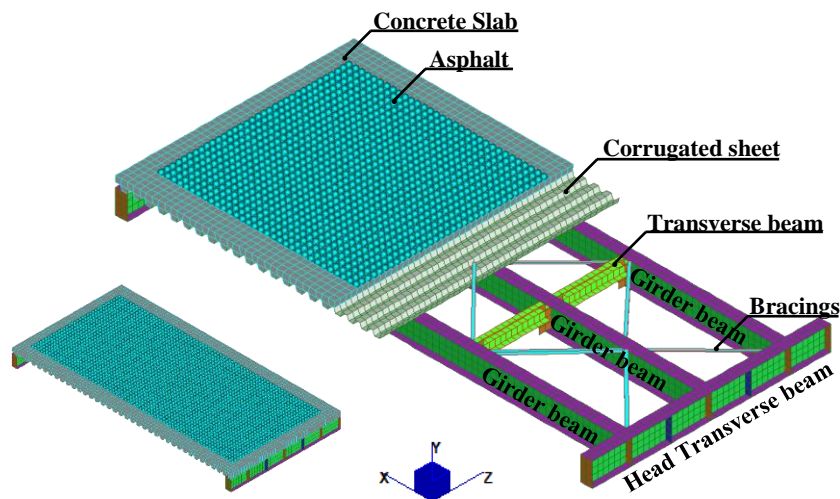
Figure 11: FE numerical model of the steel deck.

320   Three-dimensional solid 8-node brick elements were used to model the geometry

321   of the concrete slab, while bi-dimensional 4-node shell elements were used to

322   shape the geometry of the main beams, the corrugated steel sheet, and all the

323   steel stiffening plates. Since secondary crossing beams and bracings are bolted

324   to the main steel girders, these parts were introduced as beam and truss elements

325   respectively. The layer of asphalt laying above the concrete slab was defined as

326   a distributed surface mass.

327   According to what is mentioned in section 2.1, two vertical cuts were provided

328   at a fixed length of the two outer beams of the bridge model, able to simulate the

329   presence of damage. From the mechanical point of view, the two cuts strongly

330   reduced both the stiffness and the load-carrying capacity of the bridge, thus the

331   two bolted twin plate splices illustrated in Figure 5 were properly designed to

332   fully restore the original bending and shear capacity of the solid beams.

333   However, during the bridge modelling phase, since the stiffness of the bridge

334   was completely restored by the splices and the mass of the plates used for this

335   purpose is negligible compared to the whole mass of the bridge, the two splices

336   were not included in the FE model considering the outer beams as solid beams.

337   Concerning the load applied during the linear static analyses, the forces

338   computed for each load step were spread as equivalent pressures in 150x150

339   mm^2 square areas on the concrete slab of the FE model. The pressures were set

340   according to the positions of the concrete cubes used for enforcing loads on the

341   bridge beams and the load fractions defined in section 2.2.

342   The rubber bearings were modelled by using equivalent elastic springs. The

343   standards dealing with bridge bearing devices [43] and the neoprene rubber

344   datasheet [44] allowed a straight calculation of the axial stiffness value of those

345   springs, taking into consideration the incompressibility of the rubber. By

346   assuming the shear modulus G and the shape factor S of the neoprene sheets

347   respectively equal to 0.9 MPa and 2.5, the axial stiffness of the springs was

348   initially set to $7.2 \cdot 10^4$ kN/m.

349 The calibration of this parameter has played a crucial role during the model

350 updating procedure. In particular, the final value was obtained by matching the

351 experimental Load-Displacement curve measured at the support positions with

352 the results of the Linear Static analyses (LSA) carried out on the FE model. The

353 optimization procedure provided an updated value for the axial stiffness of the

354 springs equal to $6.5 \cdot 10^4$ kN/m, which was then used in the subsequent numerical

355 calculations of both static and dynamic analyses.

356 It is well known that the elastic modulus of the materials including concrete and

357 rubber, is varying according to the frequency range in which the material is

358 investigated [45, 46]. In particular, the dynamic modulus is usually greater than

359 the static one.

360 However, in the case study presented here, the structure is mainly composed of

361 steel elements, which do not change their modulus with the excitation frequency.

362 Furthermore, the investigated frequencies are in the range from 0 to 100 Hz, a

363 low-frequency interval in which the difference between static and dynamic

364 modulus can be neglected both for rubber and concrete, although the damping is

365 varying in a meaningful way. It is to remember that ultrasonic testing is in

366 general worked out with probes ranging from 10 to 60 kHz.

4 Static and dynamic investigation outcomes of the bridge model

369 The static tests allowed detecting vertical displacements near the rubber bearings

370 of the central beam, and at the mid-span of the main steel girders. In this way,

371 both the average stiffness of the support and the deck has been derived.

372   Figure 12 and Figure 13 show a very good agreement among the experimental

373   displacements and those obtained by a series of linear analyses performed by

374   gradually increasing the load applied to the model. In particular, Figure 12

375   illustrates the values of the two support deflections "*Exp_*" during the loading

376   test compared with those obtained through the numerical LSA. The calibration

377   was set by matching the black line (experimental average), with the results of the

378   central girder supports in the FE model (red line). On the other hand, the static

379   tests allowed also triggering the value of the static Young's modulus for the

380   concrete slab. The tuning of the support stiffness and the concrete elastic

381   modulus led to a very good fit among the experimental and the numerical

382   displacements on the mid-span section for all the three girders (Figure 13).
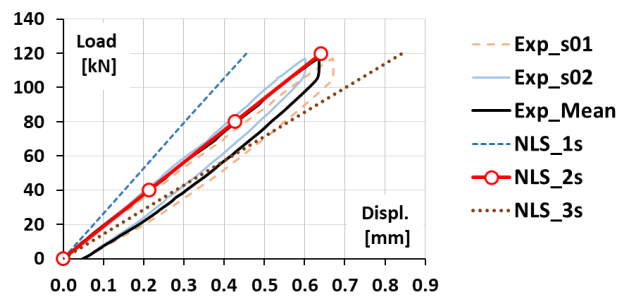
383

384   Figure 12. Plot of the Load-Displacement curve measured at the supports compared with the

385   curves of the linear static analysis performed on FE model.
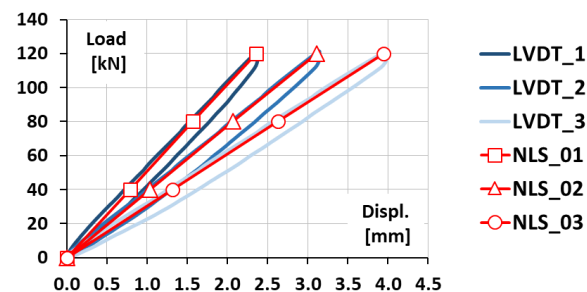
386

387   Figure 13. Plot of the Load-Displacement curve measured at the midspan of the main beams and

388   those reconstructed by performing a linear static analysis.

18

389 Once the elastic properties of neoprene rubber were calibrated, the values of the

390 mass density of both concrete and asphalt were adjusted by minimizing the

391 distance from the experimental frequencies.

392 The recorded data were processed using both the frequency and the time

393 domains. The Frequency Domain Decomposition (FDD) [11, 47] and the

394 Stochastic Subspace Identification (SSI-COV) [48, 49, 50], both available in a

395 MatLab Environment [51, 52], were applied to the recorded data.

396 As previously pointed out, the modal identification was performed by

397 considering the accelerations induced by environmental micro-tremors, hammer

398 hits and people walk. A linear detrending and a resampling up to 500 Hz were

399 applied to the recorded time series and two different output-only identification

400 algorithms were employed to obtain an estimate of natural frequencies and mode

401 shapes.

402 The vibration modes of the bridge are represented by the local maxima of the

403 first singular value (SV) line (Figure 14), obtained by processing time windows

404 of 16384 samples, considering an overlap of 50% between segments and

405 adopting a Hanning window to reduce the leakage. Then, the SSI_COV

406 algorithm was used to validate the FDD outcomes. The inputs for the SSI

407 method strongly influence their results, for this reason, they were chosen

408 accordingly to what suggested by *Magalhlaes et Al.* [49, 53]. In the present

409 application, good results were achieved with a time lag of 1 second and a model

410 order equal to 140.

411 The lowest six amplification peaks are sharply shown in Figure 14, in which the

412 first averaged normalized singular value, stable poles and the coherence are

413 identified with the black line, the aligned red circles and the grey line.

414 A coherence value higher than 0.8 means that the measured signals are well

415 correlated and thus noise shows a low influence. Instead, low coherence values

416 indicate that the signals are strongly influenced by noise. For this reason, the

417 spectrum part associated with coherence lower than 0.8 can be neglected.
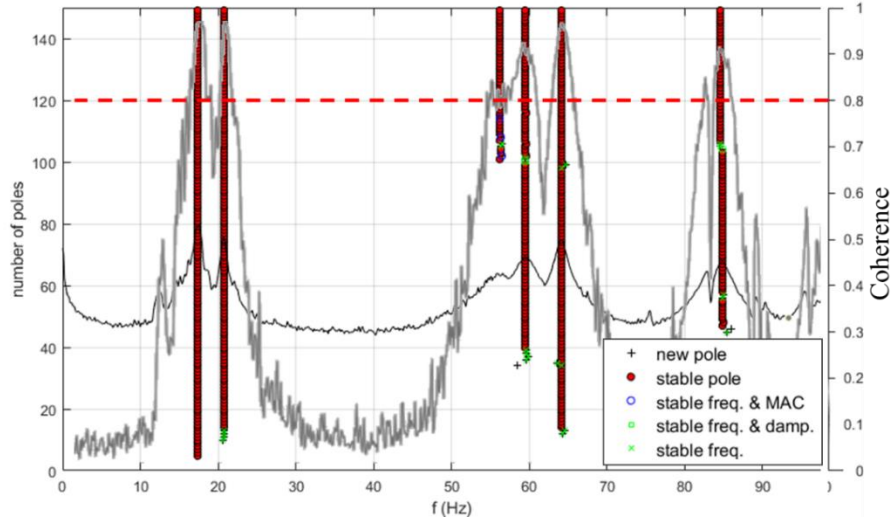
418

419 Figure 14: Plot of the first normalized singular value (black line), the SSI plot and the Coherence

420 (grey line).

421 Table 2 collects the comparison among the extracted experimental frequencies

422 and those obtained carrying out the modal analysis on the FE model. The

423 frequency values listed in Table 2 show a good agreement among numerical and

424 experimental values and a small Coefficient of Variation (CV).

425

426 Table 2. List of identified modal shapes, modal frequencies and damping ratio.

| Mode	Mode Type	FDD [Hz]	CV	SSI [Hz]	CV	Damping [%]	Numerical [Hz]	Error [-]
1	Bending	17.6	0.40%	17.6	0.21%	1.9%	17.6	0.0 %
2	Torsional	20.8	0.00%	20.8	0.08%	1.4%	20.4	1.9 %
3	Bending	59.4	-	59.5	0.23%	2.1%	51.1	13.9 %
4	Torsional	55.9	0.57%	56.8	0.11%	4.4%	51.2	8.41 %
5	Plate-like	64.2	0.11%	64.7	0.11%	0.9%	66.4	-3.43 %
6	Plate-like	85.0	0.17%	85.3	0.18%	1.4%	92.8	9.18 %

427

428 The deviations between the numerical and the experimental frequency sets are

429 lower than 10% for all but one of the modes and fit almost exactly for the first

430 two modes that were assumed as reference parameters for the damage detection.

431 Even the identified mode shapes (Figure 15), show a good agreement in

432 comparison with those obtained from the FE model Modal Analysis (Figure 16).

433 However, the 3rd mode and the 4th one appear inverted in their positions in Table

434 2 and Figure 16.
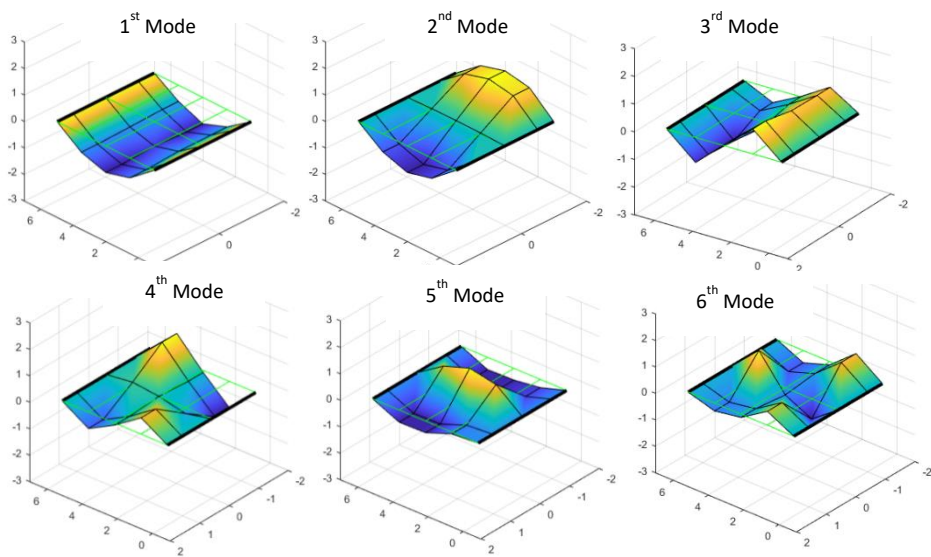
435

436   Figure 15. Lowest six mode shapes identified through the operational modal analysis.

437
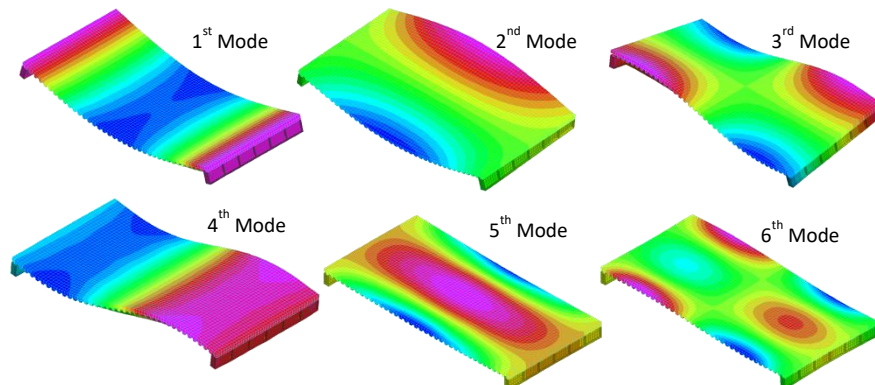
438

439   Figure 16. Lowest six mode shapes of the FE model.

440

441 The mode correspondence between the experiment and its numerical counterpart

442 can be validated through the so-called Modal Assurance Criterion (MAC):

$$MAC(\varphi_i, \varphi_j) = \frac{\left|\varphi_i^T, \varphi_j\right|^2}{\left(\varphi_i^T \varphi_i\right)\left(\varphi_j^T \varphi_j\right)} \tag{1}$$

444 By computing the MAC values of the identified mode shapes, the orthogonality

445 error of the modes can be checked (Figure 17). On the other hand, the MAC

446 cross-correlation of the numerical modal shapes with the experimental ones

447 gives a mark of the soundness of the FE model as a counterpart of the real

448 structure.
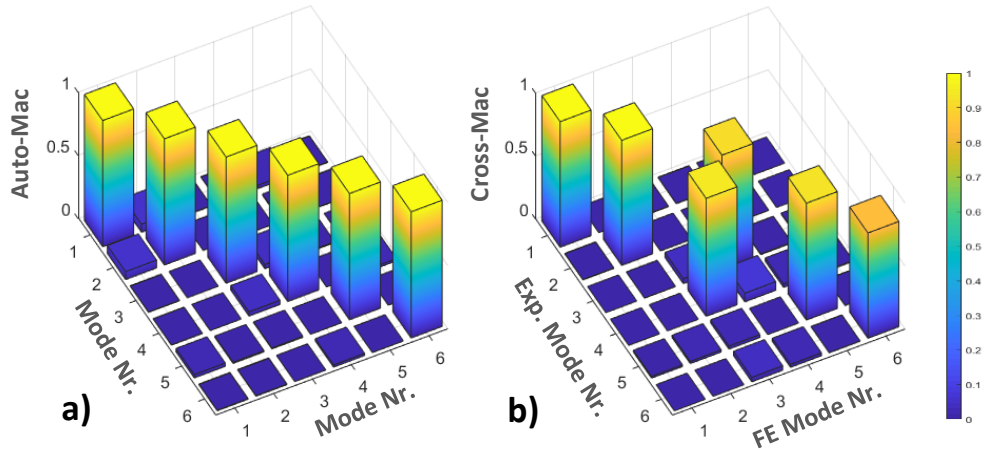
Figure 17. Bar-plots of the AutoMAC (a) and CrossMAC (b) computed on the set of the experimental modal shapes and among the experimental and numerical modal shape sets.

452 The numerical values of the CrossMAC bar chart depicted in Figure 17.b are

453 listed in the matrix of Table 3.

454 Table 3. Cross Mac values according to figure 17.b.

Mode		Calculated Modes					
		1	2	3	4	5	6
Experimental Modes	1	1.00	0.00	0.00	0.00	0.00	0.00
	2	0.00	0.99	0.00	0.00	0.00	0.00
	3	0.00	0.00	0.04	0.91	0.01	0.01
	4	0.00	0.00	0.94	0.07	0.03	0.01
	5	0.01	0.02	0.02	0.00	0.93	0.00
	6	0.00	0.00	0.04	0.02	0.00	0.84

455

5 Effects of the presence of local damages

The damage equivalent to a crack involving the flange, or the flange and the web of a beam, was obtained by removing respectively the flange bolted twin splice plates, or both the flange and the web splice plates (Figure 18).
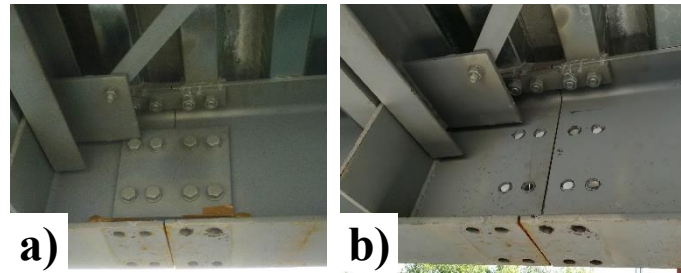

Figure 18. Progressive removal of the bolted plates: (a) removal of the bottom flange splice plates, (b) removal of flange and web splice plates.

Since the simulated damage in the beams consists of a vertical cut in the unbolted sections, this geometry change was obtained in the FE model by deleting a row of elements in the selected positions. In particular, the removal of the bolted splice plates in the bottom flange of the left side beam represents the damage phase D1; the removal of both the flange and the web splice plates of the same beam denotes the damage phase D2. By adding to this state the removal of the splice plates of the lower flange in the right side beam, the phase D3 is attained; progressing with the last web splice plates removal the maximum damage phase D4 is obtained.

The presence of the simulated damage in the numerical model was taken into account by cutting away the shell elements filling the gap between the two disconnected (unbolted) flange or web plates. For the sake of illustration, the

477   damage conditions D1 and D2 are sketched in the following figure (Figure 19),

478   by representing the portion around the cut section.
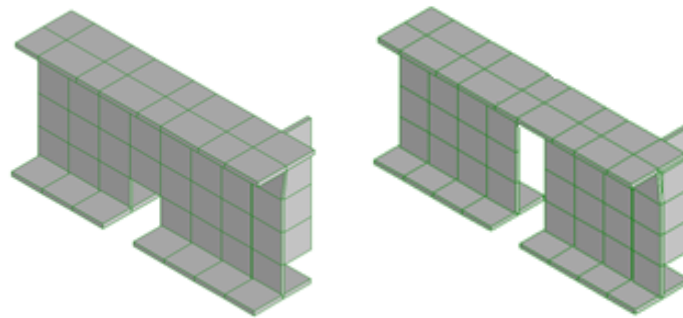
479

480   Figure 19: On the left the damaged condition D1, while, on the right, the Condition D2.

481

482   At the end of the experimental campaign, all the data of the subsequent four

483   damage phases were processed, by extracting the variations of the two lowest

484   frequencies. Then, the variations of the same frequencies were computed from

485   the model by progressively deleting the elements simulating the damages as in

486   figure 12. In this way, the data reported in Figure 20 were obtained.

487   Both the first and the second mode are very sensitive to the damage. The

488   experimental data showed an almost linear reduction in frequency with the

489   progressive severity of the damage state.

490   The FE simulation led to a very good fit between the detected frequencies with

491   those obtained performing the numerical modal analysis on the progressively

492   changed model. The relative error on all the phases remained always below 3%

493   of the experimental value. The dynamic tests were performed using only two

494   accelerometers without a roving sensor technique [54]. It allowed to sharply

495   identify only the first two natural frequencies, the decay of which is illustrated in

496   Figure 20 describing all the damage states. Since the aim of the paper concerns

497   the evaluation of the stiffness and the fundamental frequency variations due to

498   the damage level, higher modes were not taken into account. Further analyses

499   will allow observing variation related to higher frequencies and mode shapes

500   too. In particular, the analysis of higher mode shapes needs significant

501   improvements in the spatial resolution of the sensors.

502
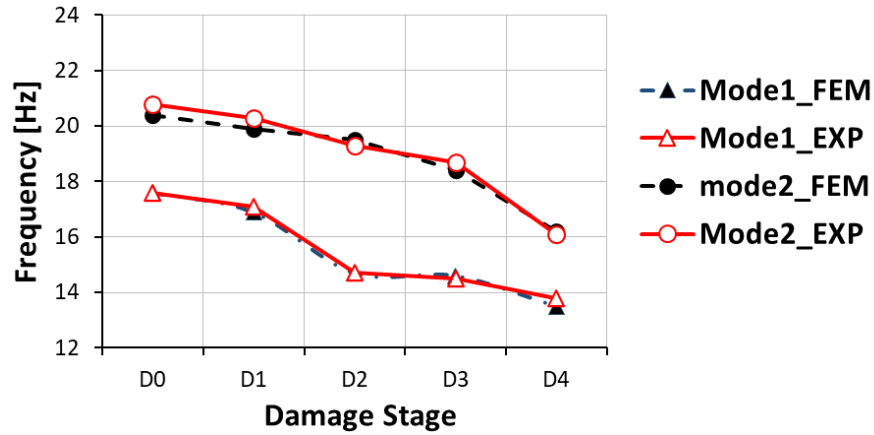
503   Figure 20. Frequency decay due to the presence of damage

504

505   Table 4. Comparison between numerical, experimental and analytical frequencies for each

506   damage phase.

Freq.	D0 [Hz]	D1 [Hz]	D2 [Hz]	D3 [Hz]	D4 [Hz]
$F_{1,exp}$	17.6	17.1	14.7	14.5	13.8
$F_{1,mod}$	17.6	16.9	14.7	14.6	13.5
$F_{1,an}$	17.6	16.4	15.7	13.1	12.0
$F_{2,exp}$	20.8	20.3	19.3	18.7	16.1
$F_{2,mod}$	20.4	19.9	19.5	18.4	16.2
$F_{2,an}$	-	-	-	-	-

507

508   Table 4 lists detected and obtained frequencies in the four increasing damage

509   states. Once the distributed mass, the bending stiffness and the torsional constant

510   were computed according to the mechanical properties of the materials and the

511   geometry of the bridge, analytical formulas for the frequencies were used in

512   validating the FE model. The results obtained by solving the closed-form

513   formulas governing the dynamic equilibrium of an equivalent beam [55, 56] are

514   very similar to the values obtained from the numerical model.

25

515   Starting from values of bending rigidity *EJ* and torsional rigidity *Gk$_t$* equal to

516    $1.35 \cdot 10^5$ *kNm^2* and $4.27 \cdot 10^4$ *kNm*, respectively, and keeping constant values of

517   distributed mass ρA and rotational inertia ρJ_p respectively equal to 916 kg/m

518   and 0.804 kNm the analytical values of the lowest bridge natural frequencies

519   can be easily computed. The frequency related to the first mode was computed

520   for all the damage states by introducing the rigidity modification for the

521   elements simulating the damaged zones. Concerning the fundamental frequency,

522   both experimental outcomes and analytical calculations correctly evaluated the

523   reduction in terms of stiffness. In particular, a decrease of 13%, 20%, 33%, and

524   40 % of total stiffness was estimated through the frequency values extracted

525   from the dynamic tests. The analytical stiffness decay computed for the damage

526   conditions D1, D2, D3, and D4, are respectively 8%, 30%, 31% and 41% with a

527   good match of the experimental values.

528

529   **6 Conclusions**

530   This paper presents detailed data of an experimental campaign carried out on a

531   1:4 scaled model of a composite steel-concrete bridge deck. In the range up to

532   100 Hz, eight vibration modes were distinctly identified. A very good agreement

533   was found between the experimental modes and those provided by the FE model

534   except for the third and fourth modes, that are switched between the experiments

535   and the calculations. The MAC computed convolving the two sets of numerical

536   and identified modal shapes showed high cross-correlation values, although a

537   swap between third and fourth mode was detected. This small misfit is probably

538   a consequence of the non-uniform thickness of the concrete deck caused by the

539   self-weight sagging of the deck during the concrete pouring operations.

540   Local damages simulated in two of the main beams produced important shifts in

541   the values of the first two main frequencies. The observed decay in terms of

542   frequency shows a high sensitivity of the fundamental frequency concerning the

543   presence of progressive damage.

544   Further analyses are in progress looking at the evolution of modal shapes and

545   damping ratios in connection to several mixed combinations of damage obtained

546   by varying the sequence of bolted cover plates removal. The investigation of the

547   retrofit of the cut beams by using carbon fibre patch repairs of the flange and

548   web discontinuities is planned in a further study on the model bridge.

549

550 7 Acknowledgements

562

563

564 8. References

565

[1]   K. L. Rens, T. J. Wipf e F. Klaiber, «Review of nondestructive evaluation techniques of civil infrastructure,» *Journal of Performance of Constructed Facilities,* 1997. DOI: 10.1061/(ASCE)0887-3828(1997)11:4(152)

[2]   D. McCann e M. Forde, «Review of NDT methods in the assessment of concrete and masonry structures,» *NDT and E International,* vol. 34, n. 2, pp. 71-84, 2001. DOI: 10.1016/S0963-8695(00)00032-3

[3]   A. Benedetti e M. Tarozzi, «Toward a quantitative evaluation of timber strength through on-site tests,» in *Advances in Engineering Materials, Structures and Systems: Innovations, Mechanics and Applications - Proceedings of the 7th International Conference on Structural Engineering, Mechanics and Computation, 2019*, Cape Town, 2019. DOI: 10.1201/9780429426506-300

[4]   A. Benedetti e M. Tarozzi, «Interpretation formulas for in situ characterization of mortar strength,» *Construction and Building Materials,* vol. 242, pp. 1-11, 2020. DOI: 10.1016/j.conbuildmat.2020.118093

[5]   G. Spencer, L. Hung Manh, L. Tuan, N. Luan, S. Ryan e P. Huy, «Nondestructive evaluation sensor fusion with autonomous robotic system for civil infrastructure inspection,» *Journal of Field Robotics,* pp. 988-1004, 2018. DOI: 10.1002/rob.21791

[6]   K. L. Rens, C. Nogueira e D. J. Transue, «Bridge management and nondestructive evaluation,» *Journal of Performance of Constructed Facilities,* vol. 19, pp. 3-16, 2005. DOI: 10.1061/(ASCE)0887-3828(2005)19:1(3)

[7]   R. Brincker, «Some Elements of Operational Modal Analysis,» *Shock and Vibration,* pp. 1-11, 2014. DOI: 10.1155/2014/325839

[8]   R. Brincker e C. E. Ventura, Introduction to Operational Modal Analysis, Wiley Blackwell, 2015.

[9]   S. R. Ibrahim, J. C. Asmussen e R. Brincker, «Modal Parameter Identification from Responses of General Unknown Random Inputs,» in *14th International Modal Analysis Conference*, Dearborn, Michigan, USA, 1996.

[10]   N. J. Jacobsen, P. Andersen e R. Brincker, «Applications of Frequency Domain Curve-fitting in the EFDD Technique,» in *Conference Proceedings of the Society for Experimental Mechanics Series, 2008, IMAC-XXVI: Conference and Exposition on Structural Dynamics - Technologies for Civil Structures*, New York, 2008.

[11]   R. Brincker, L. Zhang e P. Andersen, «Modal identification of output-only systems using frequency domain decomposition,» *Smart Materials and Structures,* vol. 10, n. 3, pp. 441-445, 2001. DOI: 10.1088/0964-1726/10/3/303

[12]   R. Brincker e L. Zhang, «Frequency domain decomposition revisited,» in *IOMAC 2009 - 3rd International Operational Modal Analysis Conference, p 615-626, 2009*, 2009.

[13]   B. Peeters e G. De Roeck, «Reference-based stochastic subspace identification for output-only modal analysis,» *Mechanical Systems and Signal Processing,* vol. 13, n. 6, pp. 855-878, 1999. DOI: 10.1006/mssp.1999.1249

[14] B. Peeters e G. De Roeck, «Stochastic System Identification for Operational Modal Analysis: A Review,» *Journal of Dynamic Systems, Measurement, and Control,* vol. 123, n. 4, pp. 659-667, 2001. DOI: 10.1115/1.1410370

[15] P. Kirkegaard e P. Andersen, «State space identification of civil engineering structures from output measurements,» in *Proceedings of the International Modal Analysis Conference - IMAC*, 1997.

[16] G. De Roeck, A. Teughels e E. Reynders, «Damage identification of civil engineering structures based on operational modal data,» in *Proceedings of the 1st International Operational Modal Analysis Conference, IOMAC*, 2005.

[17] S. W. Doebling, C. R. Farrar e M. B. Prime, «Summary review of vibration-based damage identification methods,» *Shock and Vibration Digest,* vol. 30, n. 2, pp. 91-105, 1998. DOI: 10.1177/058310249803000201

[18] F. Magalhães, A. Cunha e E. Caetano, «Vibration based structural health monitoring of an arch bridge: From automated OMA to damage detection,» *Mechanical Systems and Signal Processing,* vol. 28, pp. 212-228, 2012. DOI: 10.1016/j.ymssp.2011.06.011

[19] C. Gentile, M. Guidobaldi e A. Saisi, «One-year dynamic monitoring of a historic tower: damage detection under changing environment,» *Meccanica,* vol. 51, n. 11, pp. 2873-2889, 2016. DOI: 10.1007/s11012-016-0482-3

[20] J. Maeck e G. De Roeck, «Damage assessment using vibration analysis on the Z24-bridge,» *Mechanical Systems and Signal Processing,* vol. 17, n. 1, pp. 133-142, 2003. DOI: 10.1006/mssp.2002.1550

[21] J. Maeck, B. Peeters e G. De Roeck, «Damage identification on the Z24 bridge using vibration monitoring,» *Smart Materials and Structures,* vol. 10, n. 3, pp. 512-517, 2001. DOI: 10.1088/0964-1726/10/3/313

[22] M. Döhler, F. Hille, L. Mevel e W. Rücker, «Structural health monitoring with statistical methods during progressive damage test of S101 Bridge,» *Engineering Structures,* vol. 69, pp. 183-193, 2014. DOI: 10.1016/j.engstruct.2014.03.010

[23] C. Farrar, W. Baker, T. Bell, K. Cone, T. Darling, T. Duffey, A. Eklund e A. Migliori, «Dynamic characterization and damage detection in the I-40 bridge over the Rio Grande,» Los Alamos, 1994. DOI: 10.2172/10158042

[24] C. R. Farrar, P. J. Cornwell, S. W. Doebling e M. B. Prime, «Structural Health Monitoring Studies of the Alamosa Canyon and I-40 Bridges,» Los Alamos, 2000. DOI: 10.2172/766805

[25] P. F. Giordano e M. P. Limongelli, «Vibration-based damage identification for the S101 benchmark bridge: A comparison of indicators,» in *9th European Workshop on Structural Health Monitoring, EWSHM 2018*, Manchester, UK, 2018.

[26] D. Anastasopoulos, M. De Smedt, L. Vandewalle, G. De Roeck e E. P. Reynders, «Damage identification using modal strains identified from operational fiber-optic Bragg grating data,» *Structural Health Monitoring,* vol. 17, n. 6, pp. 1441-1459, 2018. DOI:

10.1177/1475921717744480

[27] A. Ibrahim, A. Eltawil, Y. Na e S. El-Tawil, «A Machine Learning Approach for Structural Health Monitoring Using Noisy Data Sets,» *IEEE Transactions on Automation Science and Engineering,* pp. 900-908, 2020. DOI: 10.1109/TASE.2019.2950958

[28] S. B. Beheshti Aval, V. Ahmadian, M. Maldar e E. Darvishan, «Damage detection of structures using signal processing and artificial neural networks,» *Advances in Structural Engineering,* vol. 23, n. 5, 2020. DOI: 10.1177/1369433219886079

[29] R. G. Lauzon e J. T. DeWolf, «Ambient Vibration Monitoring of a Highway Bridge Undergoing a Destructive Test,» *Journal of Bridge Engineering,* vol. 11, n. 5, pp. 602-610, 2006. DOI: 10.1061/ ASCE 1084-0702 2006 11:5 602

[30] Y. Zhou e A. Biegalski, «Investigation of large web fractures of welded steel plate girder bridge,» *Journal of Bridge Engineering,* vol. 15, n. 4, pp. 373-383, 2010. DOI: 10.1061/(ASCE)BE.1943-5592.0000111

[31] R. Haghani, M. Al-Emrani e M. Heshmati, «Fatigue-Prone Details in Steel Bridges,» *Buildings,* vol. 2, pp. 456-476, 2012. DOI: 10.3390/buildings2040456

[32] M. Chajes, D. Mertz, S. Quiel, H. Roecker e J. Milius, «Steel Girder Fracture on Delaware's I-95 Bridge over the Brandywine River,» in *Asce Structures Congress 2005*, New York, 2005. DOI: 10.1061/40753(171)36

[33] "EN 206: Concrete - Specification, performance, production and conformity".

[34] «EN 10025: Hot rolled products of structural steel».

[35] «EN 10219: Cold formed welded steel structural hollow sections».

[36] A. Tomor, J. Nichols e A. Benedetti, «Identifying The Condition Of Masonry Arch Bridges Using Cx1 Accelerometer,» in *ARCH 2016*, Wroclaw, Poland, 2016.

[37] A. Benedetti, M. Tarozzi, G. Pignagnoli e C. Martinelli, «Dynamic Investigation and Short-Monitoring of an Historic Multi-span Masonry Arch Bridge,» in *ARCH 2019*, Porto, Portugal, 2020. DOI: 10.1007/978-3-030-29227-0_92

[38] J. Nichols, A. Tomor e A. Benedetti, «Use Of Accelerometer Technology For Quantifying Condition Of Masonry Arch Bridges,» in *13th Canadian Masonry Symposium*, Halifax, CA, 2017.

[39] M. Dohler, E. Reynders, F. Magalhaes, L. Mevel, G. De Roeck e A. Cunha, «Pre- and Post-identification Merging for Multi-Setup OMA with Covariance-Driven SSI,» in *Dynamics of Bridges, Volume 5*, 2011.

[40] E. Reynders, F. Magalhaes, G. De Roeck e A. Cunha, «Merging Strategies for Multi-Setup Operational Modal Analysis: Application to the Luiz I steel Arch Bridge,» in *IMAC-XXVII*, Orlando, Florida USA, 2009.

[41] SENSR, «CX1 Network Accelerometer & Inclinometer,» [Online]. Available: https://sensr.com/downloads/R001-420-V1.0%20CX1%20Network%20Accelerometer%20and%20Inclinometer%20User%20Guid

e.pdf.

[42] I. I. a. T. ministry, Aggiornamento delle «Norme tecniche per le costruzioni», 2018.

[43] «CNR 10018/85 – Apparecchi di appoggio per le costruzioni, Istruzioni per l'impiego».

[44] F. Industriale, «Rubber sheets and mats datasheet».

[45] X. Lu, Q. Sun, W. Feng e J. Tian, «Evaluation of dynamic modulus of elasticity of concrete using impact-echo method,» *Construction and Building Materials,* vol. 47, pp. 231-239, 2013.

[46] B.-J. Lee, s.-h. Kee, T. Oh e Y.-Y. Kim, «Evaluating the Dynamic Elastic Modulus of Concrete Using Shear-Wave Velocity Measurements,» *Advances in Materials Science and Engineering,* vol. 5, pp. 1-13, 2017.

[47] R. Brincker, L. Zhang e P. Andersen, «Modal identification from ambient responses using frequency domain decomposition,» in *Proceedings of the International Modal Analysis Conference - IMAC*, 2000.

[48] F. Magalhães, Á. Cunha e E. Caetano, «Dynamic monitoring of a long span arch bridge,» *Engineering Structures,* vol. 30, n. 11, pp. 3034-3044, 2008. DOI: 10.1016/j.engstruct.2008.04.020

[49] F. Magalhães, Á. Cunha e E. Caetano, «Online automatic identification of the modal parameters of a long span arch bridge,» *Mechanical Systems and Signal Processing,* vol. 23, n. 2, pp. 316-329, 2009. DOI: 10.1016/j.ymssp.2008.05.003

[50] P. van Overschee e B. De Moor, Subspace identification for linear systems: Theory,, New York, NY: Kluwer Academic Publishers, 1996.

[51] A. Otto, «OoMA Toolbox, MATLAB Central File Exchange,» [Online]. Available: https://www.mathworks.com/matlabcentral/fileexchange/68657-ooma-toolbox.

[52] E. Cheynet, «Operational modal analysis with automated SSI-COV algorithm,» 2020. [Online]. Available: https://www.github.com/ECheynet/SSICOV.

[53] F. Magalhaes e A. Cunha, «Explaining operational modal analysis with data from an arch bridge,» *MechanicalSystemsandSignalProcessing,* vol. 25, pp. 1431-1450, 2010.

[54] J. Zhang, K. Maes, G. De Roeck, E. Reynders, C. Papadimitriou e G. Lombaert, «Optimal sensor placement for multi-setup modal analysis of structures,» *Journal of Sound and Vibration,* vol. 401, pp. 214-232, 2017. DOI: 10.1016/j.jsv.2017.04.041

[55] M. Rades, Mechanical Vibrations I, Printech, 1990.

[56] S. S. Rao, Mechanical vibrations, Prentice Hall, 2010.

566

567